

Pattern Formation and Instabilities in Particulate Suspensions

Marc A. Fardin,¹ Thibaut Divoux,^{2,3} Sungyon Lee,⁴ and Irmgard Bischofberger⁵

¹Université Paris Cité, CNRS, Institut Jacques Monod, Paris, France; email: marc-antoine.fardin@ijm.fr

²Laboratoire de Physique, CNRS, Ecole Normale Supérieure de Lyon, Lyon, France

³International Research Laboratory, CNRS, Kavli Institute for Theoretical Physics, French American Center for Theoretical Science, Santa Barbara, California, USA

⁴Department of Mechanical Engineering, University of Minnesota, Minneapolis, Minnesota, USA

⁵Department of Mechanical Engineering, Massachusetts Institute of Technology, Cambridge, Massachusetts, USA; email: irmgard@mit.edu

ANNUAL
REVIEWS **CONNECT**

www.annualreviews.org

- Download figures
- Navigate cited references
- Keyword search
- Explore related articles
- Share via email or social media

Annu. Rev. Fluid Mech. 2026. 58:275–300

First published as a Review in Advance on October 1, 2025

The *Annual Review of Fluid Mechanics* is online at fluid.annualreviews.org

<https://doi.org/10.1146/annurev-fluid-100224-111041>

Copyright © 2026 by the author(s). This work is licensed under a Creative Commons Attribution 4.0 International License, which permits unrestricted use, distribution, and reproduction in any medium, provided the original author and source are credited. See credit lines of images or other third-party material in this article for license information.



Keywords

particulate suspensions, instabilities in complex fluids, pattern growth, fluid-to-solid transition, confinement, scaling analysis, dimensionless numbers

Abstract

Particulate suspensions, consisting of solid particles dispersed in a fluid, exhibit complex flow behaviors influenced by multiple factors, including particle interactions, concentration gradients, and external forces. Suspensions play an important role in diverse processes, from sediment transport to food processing, and display instabilities triggered by shear-driven effects, frictional interactions, and viscous forces. These instabilities can often be understood by identifying the key mechanical quantities that govern the dynamics. Following hydrodynamic tradition, such mechanics can be characterized by dimensionless numbers, which encapsulate the interplay between geometric, kinematic, and mechanical factors. Many of these numbers represent competitions between opposing pairs of mechanical quantities, which we discuss in detail while also considering a few phenomena that require more complex combinations. By emphasizing the

underlying mechanical principles, this review provides a perspective for understanding pattern formation and flow instabilities in confined particulate suspensions across different flow geometries.

1. INTRODUCTION

Particulate suspensions—fluids containing dispersed solid particles—shape our world. From river sediment transport to cement slurries and food processing, suspensions of particles in liquids exhibit a vast array of complex flow behaviors. Unlike simple fluids, where the viscosity provides a straightforward description of a resistance to deformation, suspensions display additional effects arising from particle–particle or particle–wall interactions, concentration gradients, and external forces. Particulate suspensions exhibit a rich variety of pattern growth, spanning multiple physical mechanisms, as illustrated in **Figure 1**. Instabilities might be triggered by particle migration or lead to shear-induced resuspension (Shields 1936, Charru & Mouilleron-Arnould 2002, Saint-Michel et al. 2019, Di Vaira et al. 2022). In sedimenting suspensions, hydrodynamic interactions give rise to Rayleigh–Taylor-like instabilities and large-scale convective flows (Hoyal et al. 1999, Wysocki et al. 2009). In some cases, classical interfacial instabilities such as viscous fingering can be altered by the presence of particles (Kudrolli et al. 2020, Luo et al. 2020).

In a confined environment, pattern formation can arise due to the competition between interparticle forces, hydrodynamic interactions, and boundary effects. Examples include the formation of particle-rich and particle-depleted bands in shear flows, fingering patterns in confined displacement flows, and viscoelastic fracturing in yield-stress suspensions (Van Damme et al. 1994, Tirumkudulu et al. 1999, Timberlake & Morris 2002, Barral et al. 2010, Roht et al. 2018). These phenomena often give rise to patterns whose characteristic length scale may depend directly on the scale of the confinement or exhibit more complex scaling behavior including power-law dependencies modified by interfacial or elastic stresses (Eriksen et al. 2018, Divoux et al. 2020). Understanding these scaling laws is crucial for predicting pattern formation and flow transitions in confined particulate suspensions.

A first step in characterizing these systems is to quantify the relationship between the microscopic particle scale and the macroscopic flow geometry. If we call d the size of the particles and D the characteristic size of the flow geometry (recurring symbols are summarized in **Table 1**), then their ratio, $N_0 \equiv d/D$, provides a dimensionless measure separating the macroscopic and microscopic scales. In standard fluids, the size difference between the macroscopic scale and the molecular constituents is so large that the microscopic scale is not explicitly taken into account. In these cases, we have $d \ll D$ and $N_0 \simeq 0$. In the other limit, the size of the particles is bounded by the size of the geometry, $d \lesssim D$. In this review, we focus on flows of fluids containing particles of significant size but still sensibly smaller than the macroscopic scale, so we have $0 < N_0 < 1$, an inequality that can be refined further.

The number N_0 provides a useful dimensionless metric, but it is usually superseded by a measure of the concentration of particles, commonly expressed as the particle volume fraction ϕ . For a flow geometry with a single characteristic dimension, the particle volume fraction is related to the macroscopic and microscopic scales by $\phi \propto N_p d^3 / D^3 \propto N_p N_0^3$, where N_p is the number of particles. The particle volume fraction is necessarily smaller than 1, providing a stronger bound on N_0 , since $\phi \lesssim 1 \rightarrow N_0 \lesssim N_p^{-1/3}$. In the idealized case of identical hard spheres, the maximum volume fraction ϕ_m is 0.74, corresponding to the densest crystal packing. A random close packing of spheres yields a volume fraction of 0.64, and a loose packing obtained from slow settling of spheres

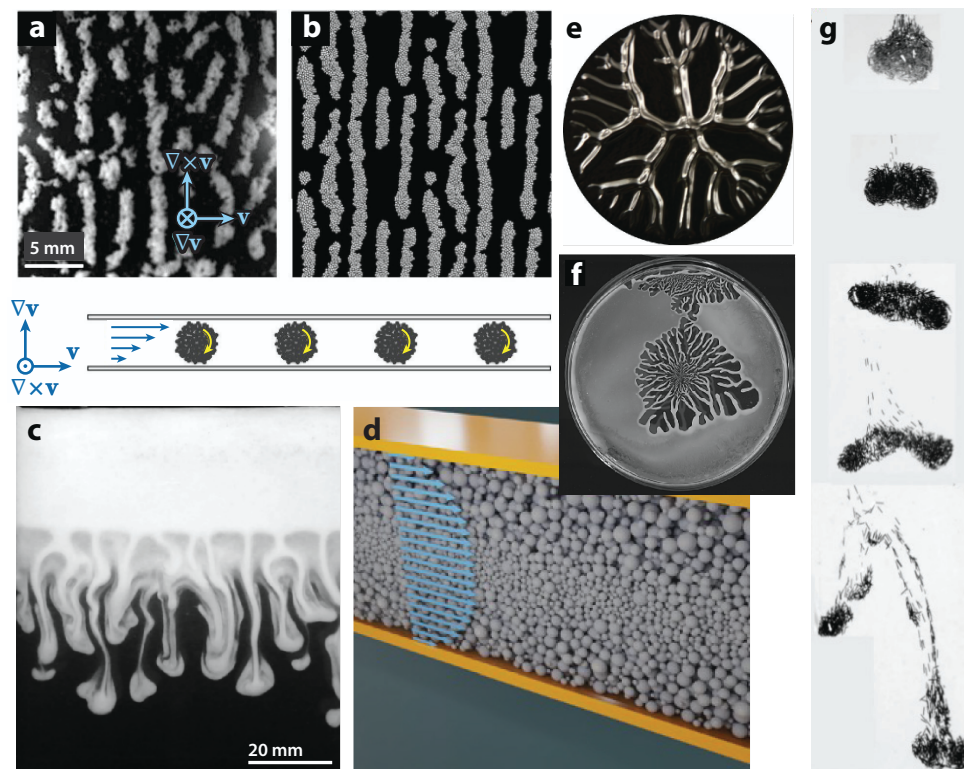


Figure 1

Vorticity-aligned log-rolling structures obtained from (a) experiments and (b) simulations by shearing attractive particles in confined gaps. The horizontal direction corresponds to the velocity direction v and the vertical direction to the vorticity direction $\nabla \times v$ so that the flow-gradient direction ∇v is perpendicular to the images. The sketch below panels *a* and *b* shows the geometry of the array of log-rolling flocs in the velocity–velocity gradient plane. Panels *a* and *b* adapted from Varga et al. (2019). (c) Rayleigh–Taylor-like instability in a suspension of glass beads in a glycerol–water mixture. Panel adapted with permission from Guo et al. (2024). (d) Shear-induced migration in a polydisperse particle suspension in pressure-driven, planar channel flow. Panel adapted from Di Vaira et al. (2022) (CC BY 4.0). (e) Pattern resulting from a fingering instability in a carbon black gel; experiments were performed in a parallel-plate geometry (diameter 40 mm), where the upper plate was lifted at a constant speed. Panel adapted from Divoux et al. (2020). (f) Pattern formed by dewetting of a cornstarch suspension. The diameter of the petri dish is 10 cm. Panel adapted with permission from Habibi et al. (2012). (g) Evolution of a sedimenting cloud composed of rigid fibers at a volume fraction of approximately 5%. The scale is given by the rigid fibers, whose length is 1.2 mm. Panel adapted with permission from Park et al. (2010).

yields 0.56 (Dullien 2012). The shape of the particles, their rigidity or softness, and whether they are attractive or repulsive influence the maximum volume fraction of a system (Vlassopoulos & Cloitre 2014, Kawasaki et al. 2015, Gilbert et al. 2022). The approach to ϕ_m is associated with significant changes to the mechanical properties of a suspension (Mueller et al. 2010, Guazzelli & Pouliquen 2018). We will see that these changes can have a significant impact on the flows and instabilities in particulate suspensions.

In the study of suspensions, geometric considerations alone already yield three dimensionless numbers, N_0 , N_p , and ϕ . For the simplest flow geometries, we have $0 < N_0 < (\phi_m/N_p)^{\frac{1}{2}}$, which sets bounds on the particle size, since $d = DN_0$. Should we expect qualitative differences in

Table 1 Recurring symbols

Symbol	Dimensions	Usage
d	\mathcal{L}	Particle size
D	\mathcal{L}	Main macroscopic confining dimension
W, R	\mathcal{L}	Additional macroscopic lengths (width, radius)
λ	\mathcal{L}	Characteristic length scale of pattern
ℓ	\mathcal{L}	Unspecified length scale
$\ell_{Q_1 Q_2}$	\mathcal{L}	Mechanical length built from the quantities Q_1 and Q_2 , defined if $[Q_1/Q_2] = \mathcal{L}^x$; e.g., $\ell_{\Psi\Gamma} \equiv (\Gamma/\Psi)^{\frac{1}{2}}$
ω	\mathcal{T}^{-1}	Frequency
$\dot{\gamma}$	\mathcal{T}^{-1}	Shear rate
v	$\mathcal{L}\cdot\mathcal{T}^{-1}$	Flow velocity
q	$\mathcal{L}^3\cdot\mathcal{T}^{-1}$	Volumetric flow rate
a	$\mathcal{L}\cdot\mathcal{T}^{-2}$	Acceleration
g	$\mathcal{L}\cdot\mathcal{T}^{-2}$	Effective gravitational acceleration
ρ_p, ρ_f, ρ_b	$\mathcal{M}\cdot\mathcal{L}^{-3}$	Densities (of particle, fluid, or gas bubble)
η	$\mathcal{M}\cdot\mathcal{L}^{-1}\cdot\mathcal{T}^{-1}$	Viscosity
E	$\mathcal{M}\cdot\mathcal{L}^2\cdot\mathcal{T}^{-2}$	Energy (e.g., thermal)
F	$\mathcal{M}\cdot\mathcal{L}\cdot\mathcal{T}^{-2}$	Force (e.g., particle interaction)
Γ	$\mathcal{M}\cdot\mathcal{T}^{-2}$	Surface tension
Σ	$\mathcal{M}\cdot\mathcal{L}^{-1}\cdot\mathcal{T}^{-2}$	Elastic modulus/pressure/stress (e.g., yield stress)
Ψ	$\mathcal{M}\cdot\mathcal{L}^{-2}\cdot\mathcal{T}^{-2}$	Force density, often a weight density $\Psi = \rho g$
N_0	\emptyset	Degree of confinement, $N_0 \equiv d/D$
N_p	\emptyset	Number of particles
ϕ (ϕ_m)	\emptyset	Volume fraction (maximum volume fraction)
M	\emptyset	Mobility ratio, $M \equiv \eta_1/\eta_2$
$N_{Q_1 Q_2}$	\emptyset	Dimensionless number corresponding to Q_1 and Q_2 and using d as length scale

behavior by varying the particle size within these bounds? Indeed, mechanics provides a different way to approach geometry, revealing less visible but nonetheless discernible boundaries. One such boundary is that separating Brownian and non-Brownian regimes. At room temperature and under nominal gravity, particles are non-Brownian if they are larger than approximately 1 μm . This threshold is obtained by comparing the thermal energy and the force density Ψ . The thermal energy is $E \equiv k_B T$, with k_B the Boltzmann constant and T the temperature, and has the dimensions $[E] = \mathcal{M}\cdot\mathcal{L}^2\cdot\mathcal{T}^{-2}$. The force density is a weight density ρg , where ρ is the effective density taking into account buoyancy, and g is the effective acceleration. The force density has the dimensions $[\Psi] = \mathcal{M}\cdot\mathcal{L}^{-2}\cdot\mathcal{T}^{-2}$. The dimension of the ratio between thermal energy and force density is purely spatial, $[E/\Psi] = \mathcal{L}^4$, and $\ell_{\Psi E} \equiv (E/\Psi)^{\frac{1}{4}}$ represents a length scale resulting from mechanical considerations. Particles of a size smaller than this length scale are dominated by thermal effects (i.e., Brownian dynamics if $d < \ell_{\Psi E}$), and particles of a size larger than this length scale are dominated by gravitational effects (i.e., non-Brownian dynamics if $d > \ell_{\Psi E}$). In this review, we mainly focus on suspensions of non-Brownian particles, a condition that can be written as $N_{\Psi E} > 1$, where $N_{\Psi E} \equiv (d/\ell_{\Psi E})^4 \equiv \Psi d^4/E$ is the dimensionless number built by comparing d and $\ell_{\Psi E}$.

Instabilities in suspensions can be influenced by a number of forces. Rigorously, a force is a quantity with the dimensions $\mathcal{M}\cdot\mathcal{L}\cdot\mathcal{T}^{-2}$. Colloquially, the term is routinely used to more broadly

refer to a larger class of mechanical quantities with dimensions of the form $\mathcal{M}\cdot\mathcal{L}^x\cdot\mathcal{T}^y$ (Fardin et al. 2024). We have mentioned that the flow of a suspension can depend on a force density Ψ and a thermal energy E , but a surface tension Γ ($\mathcal{M}\cdot\mathcal{T}^{-2}$), a stress Σ ($\mathcal{M}\cdot\mathcal{L}^{-1}\cdot\mathcal{T}^{-2}$), an interaction force F ($\mathcal{M}\cdot\mathcal{L}\cdot\mathcal{T}^{-2}$), a density ρ ($\mathcal{M}\cdot\mathcal{L}^{-3}$), and a viscosity η ($\mathcal{M}\cdot\mathcal{L}^{-1}\cdot\mathcal{T}^{-1}$) could be relevant parameters as well. A wide variety of phenomena can be observed, depending on the prevalence of some of these quantities over others. A single review cannot cover the full diversity of situations. Nevertheless, we hope readers and future researchers will not be discouraged by the complexity of the parameter space. Instead, we view this vast landscape as an exciting frontier for exploration, where surprises are waiting and new insights are ready to be uncovered. In this spirit, we advocate for an approach based on scaling and dimensional analysis to navigate the complexity. Considering the interplay of pairs of mechanical quantities already provides insight into the mechanisms underlying a number of flow instabilities, revealing recurring patterns across seemingly disparate systems. Further research on the crossovers between different flow regimes may provide an even richer picture based on dimensionless numbers combining more than two mechanical quantities at a time.

The review is structured as follows: In Section 2, we revisit the construction of dimensionless numbers that are involved in pattern formation in particulate suspensions, offering a fresh perspective on the underlying mechanics. We then focus on a canonical flow configuration—fluid invasion in a Hele–Shaw cell—in Section 3, which provides a simple yet rich setting for observing a variety of interfacial patterns and instabilities. In Section 4, we zoom in on a specific dimensionless number, revisiting key physical scenarios and pattern formation where it plays a role, including sediment transport, bubbles in suspensions, and suspension flow down an incline. Last, in Section 5, we explore the interplay between nonlinear rheology and pattern formation, considering more complex cases where suspensions undergo state transitions, such as liquid-to-solid transitions due to jamming or drying, or solid-to-liquid transitions driven by shear-induced yielding.

2. GENEALOGY OF DIMENSIONLESS NUMBERS

Different flow regimes emerge depending on the predominant mechanical quantities in a specific setting. For instance, we used the dimensionless number $N_{\Psi E}$ to delineate Brownian and non-Brownian regimes depending on the relative importance of thermal energy E and force density Ψ for a particle of size d . To facilitate the discussion of more complex phenomena with multiple relevant mechanical quantities, we adapt the recently introduced notation where the dimensionless number associated with a pair of mechanical quantities Q_1 and Q_2 is simply written as $N_{Q_1 Q_2}$, as we did in $N_{\Psi E}$ (Fardin et al. 2024). The order of the indices is irrelevant: $N_{Q_1 Q_2} = N_{Q_2 Q_1}$. The sidebar titled A Dimensionless Juggle illustrates why this notation can simplify the discussion.

2.1. Comparing Length Scales

The comparison between the microscopic size d and the macroscopic size D , encompassed in N_0 , is straightforward. With $\ell_{\Psi E}$, we have seen that mechanics can generate other less obvious length scales. In suspension flows, regimes can be defined by comparing either the particle size d or a macroscopic length D to length scales derived from mechanics. We adopt the notation that numbers of the form $N_{Q_1 Q_2}$ are defined using the particle size d , and we use the translation factor $N_0 \equiv d/D$ if a macroscopic number is the relevant one for the phenomenon.

Many dimensionless numbers based on ratios of the form $d/\ell_{Q_1 Q_2}$ can be formed. Indeed, when two mechanical quantities share the same exponent of the time dimension, their ratio leads to a length scale. This is in particular the case for any pair chosen from a force density Ψ , a stress Σ ,

A DIMENSIONLESS JUNGLE

For historical reasons, a zoo of dimensionless numbers has been introduced over the last century, including some that have multiple competing names. For instance, the dimensionless number $N_{\Psi\Gamma} \equiv \Psi d^2/\Gamma$ may be called the Eötvös number or the Bond number (Catchpole & Fulford 1966). Moreover, dimensionless numbers are defined modulo an overall power, and one might encounter the Jesus number (Vogel 1988), which is the inverse of the Bond number, or the Goucher and Derjaguin numbers, which are the square root of the Bond number (Catchpole & Fulford 1966). Usually, these similar numbers are expressed by using the first two letters of the associated names, so one may write $E_o = B_o = J_e^{-1} = G_o^2 = D_e^2$. Our suggested notation avoids confusion by systematically defining the number $N_{Q_1Q_2}$ in such a way that the mechanical quantities have the smallest integer exponents (Fardin et al. 2024); thus, we write $N_{\Psi\Gamma} \equiv \Psi d^2/\Gamma$ and not $d(\Psi/\Gamma)^{\frac{1}{2}}$. The notation also has the benefit of placing numbers that have been historically favored, such as $N_{\Psi\Gamma}$, on an equal footing with numbers like $N_{\Psi E}$ and $N_{\Gamma E}$ that—to our knowledge—do not have standard names but are nonetheless important. The tree in **Figure 2** illustrates the multiplicity of names associated with some of the most frequent duos of mechanical quantities encountered in fluid dynamics.

a surface tension Γ , a force F , or an energy E , since all these mechanical quantities have dimensions of the form $\mathcal{M}\cdot\mathcal{L}^x\cdot\mathcal{T}^{-2}$. Ten pairs, and thus 10 length scales, can be defined from these five mechanical quantities alone. Would we then need to consider 10 dimensionless numbers? Considering the five mechanical quantities in addition to d and D , the Buckingham π theorem reveals that only four dimensionless numbers are required. But which ones? The theorem does not provide guidelines on how to construct and choose these dimensionless numbers. Why should, for instance, $N_{E\Psi}$ be favored over, say, $N_{E\Gamma}$? Which principles can guide the selection of dimensionless numbers?

The mechanical length scales associated with the same set of mechanical quantities are related to each other. For instance, we have

$$\ell_{\Psi E} = (\ell_{\Psi\Gamma}\ell_{\Gamma E})^{\frac{1}{2}}. \quad 1.$$

The length scale $\ell_{\Psi E}$ is equal to the geometric mean between the capillary length $\ell_{\Psi\Gamma}$ and the Scheludko–Vrij length $\ell_{\Gamma E} \equiv (E/\Gamma)^{\frac{1}{2}}$ (Fardin et al. 2024). This identity implies that $N_{\Psi E} = N_{\Psi\Gamma}N_{\Gamma E}$. Relationships like this abound and rationalize why the number of dimensionless numbers can be reduced. In the example, one may reduce $N_{\Psi E}$ to $N_{\Psi\Gamma}$ and $N_{\Gamma E}$, just as much as one may choose to eliminate $N_{\Psi\Gamma}$ or $N_{\Gamma E}$. This liberty can be quite confusing at times since flow-state diagrams may be constructed using one pair of dimensionless numbers in one situation but a different pair in another. We hope that the index notation can facilitate translation between perspectives.

2.2. Kinematic Comparisons

So far, we have constructed dimensionless numbers by considering ratios of length scales. More generally, they can be constructed from kinematic rather than geometric quantities. The most famous example is the Reynolds number, generally defined as

$$\text{Re} \equiv \frac{\rho\ell v}{\eta}. \quad 2.$$

This expression involves two mechanical quantities, the density ρ and the viscosity η , as well as a length scale ℓ and a velocity v . In the context of suspensions, we define the Reynolds number using $\ell = d$.

Reynolds number:
balance between
density and viscosity;
 $N_{\eta\rho} \equiv \frac{\rho d v}{\eta}$

different forms, for example,

$$\text{Reynolds number} \quad \text{Re} \equiv \frac{\rho}{\eta} \ell v, \quad 3.$$

$$\text{Taylor number} \quad \text{Ta} \equiv \frac{\rho}{\eta} \ell^{\frac{3}{2}} a^{\frac{1}{2}}, \quad 4.$$

$$\text{Womersley/Roshko number} \quad \text{Ro} \equiv \frac{\rho}{\eta} \ell^2 \omega, \quad 5.$$

$$\text{Bagnold number} \quad \text{Ba} \equiv \frac{\rho}{\eta} \ell^2 \dot{\gamma} \tilde{\phi}, \quad 6.$$

where the kinematic dimensions of the ratio $[\eta/\rho] = \mathcal{L}^2 \cdot \mathcal{T}^{-1}$ are expressed with different kinematic quantities. The Taylor number uses a length scale and an acceleration, a , $\mathcal{L}^2 \cdot \mathcal{T}^{-1} = \mathcal{L}^{\frac{3}{2}} \cdot (\mathcal{L} \mathcal{T}^{-2})^{\frac{1}{2}}$, revealing its origin from studies of flows between concentric cylinders with $a \propto v^2/R$, where R is the radius of curvature, v the cylinder velocity, and ℓ the gap spacing (Taylor 1923, Fardin et al. 2014). The Womersley/Roshko number, derived in the context of oscillatory flows, uses an oscillation frequency ω (Roshko 1954, Womersley 1955). In the Bagnold number, used in granular flows, the characteristic length scale is the particle size $\ell = d$, $\dot{\gamma}$ is a shear rate, and $\tilde{\phi} \equiv ((\phi_m/\phi)^{\frac{1}{2}} - 1)^{-1}$ expresses the proximity to the maximum packing fraction ϕ_m (Bagnold 1954). All these numbers share the same visco-inertial root.

The kinship between flows and flow instabilities can be based on the underlying mechanical quantities. In reviewing the recent work on instabilities in flows of suspensions, we tried to keep this organizing principle in mind. Two phenomena described with dimensionless numbers sharing the same mechanical quantities are then considered more alike than if the mechanical quantities were different. From that standpoint, the Reynolds number is, for instance, considered closer to the Taylor number than to the Weissenberg number; that is, $(\rho/\eta)(\ell v)$ is considered closer to $(\rho/\eta)(\ell^3 a)^{\frac{1}{2}}$ than to $(\eta/\Sigma)(v/\ell)$.

3. MANY IN ONE: REGIMES OF INSTABILITIES FOR FLUID INVASION IN CONFINED GEOMETRIES

The displacement of a fluid by another one between two parallel plates—a setup known as a Hele–Shaw cell—is a canonical flow configuration that produces a rich variety of interfacial patterns with very simple ingredients. Perhaps the most celebrated interfacial pattern results from the viscous-fingering instability (also known as the Saffman–Taylor instability) that occurs when a less viscous (invading) fluid displaces a more viscous (defending) fluid inside a Hele–Shaw cell with plate spacing D (Saffman & Taylor 1958). The displacement is unstable when the mobility ratio M , defined as the ratio of the viscosity of the defending fluid and that of the invading fluid, is greater than one. In Newtonian fluids, this instability leads to intricate fingering patterns (Homsy 1987, Bischofberger et al. 2014). The same instability also occurs when one of the plates of the Hele–Shaw cell containing a viscous liquid is lifted, which causes the surrounding air to be drawn in and displace the viscous liquid (Derks et al. 2003, Nase 2011, Divoux et al. 2020).

Replacing the defending fluid with a particulate suspension introduces a new array of mechanical quantities, stemming from friction, shear-induced migration, and shear-induced fluidization. This leads to new interfacial patterns that are inaccessible without the presence of particles. A diverse range of regimes emerges by varying the particle volume fraction ϕ , the volumetric fluid injection rate q , or mechanical properties that affect the flow. These include the force density Ψ ,

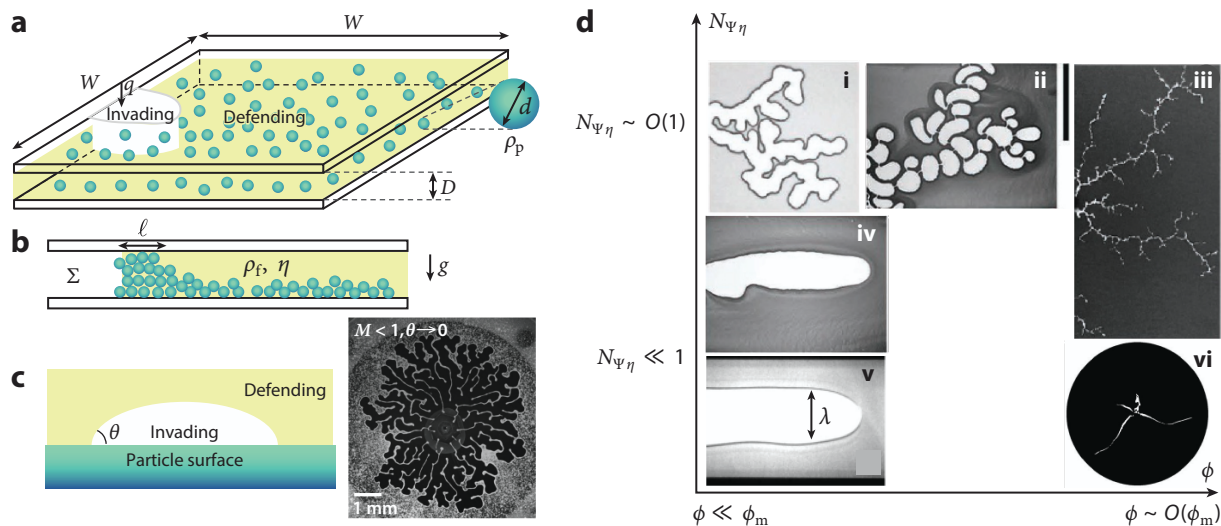


Figure 3

(a) Schematic of an invading fluid displacing a defending fluid that comprises particles inside a Hele–Shaw cell. (b) Side-view schematic of fluid invasion with heavy particles that settle to the bottom surface. (c) The contact angle θ with the particle is defined through the invading fluid submerged in the defending fluid. Panel adapted with permission from Bihi et al. (2016). (d) State diagram in terms of the particle volume fraction ϕ and $N_{\Psi\eta}$ comparing the timescale of particle transport and that of particle settling. Subpanels *i–iv* adapted with permission from Sandnes et al. (2011) (CC BY-NC-SA 3.0), subpanel *v* adapted with permission from Chevalier et al. (2007), and subpanel *vi* adapted from Ozturk et al. (2020) (CC BY 4.0).

the inertia encapsulated in the density ρ , the surface tension Γ , or a relevant measure of stress Σ , for instance, in fluids with a yield or frictional stress.

3.1. Viscosity-Dominated Regime

When air displaces a particle suspension inside a Hele–Shaw cell where the initial volume fraction of particles ϕ is far below that denoting the jamming transition, the primary effect of suspended particles on the interfacial pattern is via rheological changes in the defending fluid. For instance, air injection into a horizontal Hele–Shaw cell containing a suspension of silicone oil and density-matched polystyrene particles leads to viscosity-driven air fingering (Chevalier et al. 2007). Reminiscent of the classical Saffman–Taylor instability (**Figure 3d, subpanel v**), as long as $N_0 \ll 1$, the width λ of the stable air finger is well-described by $(W/D)^2 N_{\Gamma\eta}$, where W is the channel width and the capillary number $N_{\Gamma\eta} \equiv \eta v / \Gamma$ is based on the finger velocity v and accounts for the effective viscosity $\eta(\phi)$ of the suspension. As N_0 is increased above 0.1, however, λ deviates from the classical fingering result, suggesting that the discrete nature of particles may affect the finger width. Similarly, when a viscous oil displaces a suspension of the same oil and polystyrene particles inside a Hele–Shaw cell, the delayed onset of miscible fingering matches that of the pure liquid counterpart in the limit of $N_0 \ll 1$ but strongly deviates as N_0 is increased (Luo et al. 2020).

Even as one moves away from density-matched spherical particles, the general agreement between the behavior of a particulate system and the pure liquid counterpart persists under specific conditions. When air is radially injected into a shear-thickening cornstarch suspension inside a Hele–Shaw cell, viscous fingers with rounded fingertips form for all particle volume fractions at low pressures and at all injection pressures, as long as ϕ is below the unstressed jamming volume fraction by at least 11% (Ozturk et al. 2020).

For heavy glass spheres ($\rho_p > \rho_f$) that settle out of the defending liquid and accumulate at the advancing interface, the viscosity-dominated regime can be reached if the injection rate q is large enough to keep the particles suspended in the fluid. A transition from a friction-dominated to a viscosity-dominated regime occurs when $q > q_c$, where q_c is the critical flow rate necessary to fluidize the packed granular medium close to the moving interface (Sandnes et al. 2011). The critical flow rate q_c can be formulated based on the pressure drop for a flow through a packed granular bed (known as the Kozeny–Carman relation) to overcome the interparticle friction (Kozeny 1927, Kozeny-Carman 1937):

$$q_c \propto \lambda D \frac{\Psi}{\eta} \frac{\mu k}{\xi} \propto \lambda D d^2 \frac{\Psi}{\eta}, \quad 7.$$

where $\Psi \equiv (\rho_p - \rho_f)g$ is the force density, η is the fluid viscosity, and $k \propto d^2$ denotes the permeability of the packed bed. The dimensionless coefficients μ and ξ correspond to the effective granular friction and to the porosity. These coefficients are of order 1 and are neglected on the right-hand side of Equation 7. When q exceeds q_c , the familiar viscous fingering of pure fluids is recovered (**Figure 3d, subpanel iv**), as the entire granular suspension is mobilized via resuspension of the particles in the fluid, even away from the interface. Equation 7 can be further simplified by considering $\lambda \propto D$ and $q \propto vD^2$, which yields $N_{\Psi\eta} = q_c/q \propto \Psi d^2/(\eta v)$, where v is the characteristic flow velocity. The threshold between the frictional and the viscous regimes can then be expressed as $N_{\Psi\eta} \propto 1$. Interestingly, as friction is caused by the weight of the particles that settle and establish frictional contact with each other and with the plate, $N_{\Psi\eta}$ can be also obtained by comparing the timescale of particle settling to that of particle advection by the flow. Note that $N_{\Psi\eta}$ is discussed in more detail in Section 4.

Overall, viscosity contributes to the threshold of instabilities and to the emerging patterns in at least two ways: when it combines with surface tension, appearing in the capillary number $N_{\Gamma\eta}$, or when it combines with the force density as encapsulated in $N_{\Psi\eta}$. These viscosity-dominated regimes in particulate suspensions seem to occur under one key condition: The particles must remain well-lubricated to minimize frictional contacts both between themselves and with the walls. This condition requires a sufficiently low ϕ and sufficiently large q or, equivalently, taking the limit $N_{\Psi\eta} \ll 1$. Notably, this limit $N_{\Psi\eta} \ll 1$ can be achieved either by using density-matched particles (i.e., $\Psi \approx 0$) or by setting $q \gg q_c$ for heavy particles.

3.2. (Locally) Friction-Dominated Regime

For heavy grains that settle out of the defending liquid, the contact between particles and the bottom surface ensures the dominance of friction over viscosity for a large range of $\phi < \phi_m$ and $q < q_c$, as mentioned in Section 3.1 (Sandnes et al. 2011, Eriksen et al. 2018, Flekkøy et al. 2023, Zhang et al. 2023). As illustrated in **Figure 3b**, the settled particles form a compaction layer with a characteristic length ℓ near the advancing interface that bridges the cell gap, imposing a frictional stress $\Sigma \propto \Psi D[\exp(\ell/D) - 1]$ based on a Janssen model (Janssen 1895), where $\Psi = (\rho_p - \rho_f)g$. This ensures that the resultant displacement pattern is now governed locally by the effects of capillarity and friction in competition with the injection pressure. Once friction becomes the dominant force near the interface, the mechanism of fluid displacement becomes localized and deviates from that governing the Saffman–Taylor instability.

Even within the friction-dominated regime, interfacial patterns undergo transitions depending on the particle volume fraction ϕ . At relatively low ϕ , a frictional finger with a constant width λ forms, as shown in **Figure 3d, subpanel i** (Sandnes et al. 2011). This constant finger width has recently been theoretically rationalized by minimizing the pressure drop $\Delta\Sigma$ across the fingertip, which accounts for both frictional and capillary pressures: $\Delta\Sigma = \Psi\ell + \Gamma\kappa$, where κ (\mathcal{L}^{-1}) is

the curvature of the fingertip and Ψ ($\mathcal{M} \cdot \mathcal{L}^{-2} \cdot \mathcal{T}^{-2}$) is a friction coefficient (Flekkøy et al. 2023). The effects of hydrostatic pressure have been added by tilting the Hele–Shaw cell to a shallow inclination angle, introducing another contribution to the force density where g takes into account the inclination angle (Eriksen et al. 2018). If the force density Ψ is solely a weight density, we have seen that combining Ψ with surface tension yields the capillary length $\ell_{\Psi\Gamma} \equiv (\Psi/\Gamma)^{\frac{1}{2}}$ and the Bond number $D^2\Psi/\Gamma = N_0^{-2}N_{\Psi\Gamma}$, here defined using the macroscopic length. When the force density also includes contributions from friction, the Bond number has been termed the capillary bulldozing number (Thorens et al. 2023).

Upon further increase in ϕ , the dynamics of fluid invasion becomes intermittent (Sandnes et al. 2011): The interface remains stationary for an extended period of time, during which air gets compressed by the continuous motion of the syringe pump, causing the pressure to build up. Only when the air pressure becomes sufficiently large to overcome both frictional and capillary stresses does the air burst through the weakest point of the interface, forming a bubble termed a stick-slip bubble.

Due to its localized nature, frictional fingering can occur even without a destabilizing mobility ratio $M > 1$. The case of radially injecting water or a water/glycerol mixture into a layer of dry hydrophobic particles has been investigated, with air acting as the defending fluid (Zhang et al. 2023). In this viscously stable scenario ($M < 1$), dry particles accumulate near the moving front, forming a compacted layer that spans the plate spacing D . Consequently, similar to the $M > 1$ case, a frictional finger emerges with a characteristic width $\lambda \propto (\ell_{\Gamma\Sigma}D)^{\frac{1}{2}}((1-\phi)/\phi)^{\frac{1}{2}}$. The finger width is here related to the mechanical length $\ell_{\Gamma\Sigma} \equiv \Gamma/\Sigma$, where the surface tension Γ faces the frictional force per unit area $\Sigma \propto (D/\ell)\Sigma_t$, a stress set by the minimum pressure at the fingertip Σ_t required to overcome both friction and capillarity. One distinguishing feature is that Σ_t decreases relative to the injection pressure due to the viscous pressure gradient within the growing finger. This reduction can lead to the formation of secondary fingers sprouting from an existing one before Σ_t drops further. The onset of such branching can be described by the dimensionless viscous deformability N_{visc} :

$$N_{\text{visc}} \propto \frac{\eta}{\Sigma_b} \frac{qL}{\lambda D^3}, \quad 8.$$

where L is the finger length, and Σ_b represents the additional pressure required to form a new finger from a static side wall due to the enhanced friction. N_{visc} compares the viscous pressure drop to the frictional resistance along the side walls of a finger of length L . Based on dimensional considerations, this number may be related to a Bingham-like number $\Sigma/(\eta\dot{\gamma}) \equiv N_{\eta\Sigma}^{-1}$.

3.3. Capillarity-Dominated Regime

Even in the frictional regime, surface tension plays a role in selecting the finger width. What is missing from the previous discussion is the role of particle wettability, expressed by the contact angle between the particle surface and the invading fluid θ (Figure 3c), as the work discussed so far uses particles that are only weakly wetting or nonwetting to the invading fluid. Varying θ toward the wetting regime can modify the invasion pattern. Simulations of water radially displacing a suspension of slightly heavy particles and oil report a transition from cavity expansion and fracturing to capillary-driven displacement, occurring as θ decreases from nonwetting to water to strong imbibition (wetting to water) (Meng et al. 2020). For suspensions with a volume fraction ϕ below the jamming limit, the invading front advances via capillary compaction in the capillary-dominated regime, where particles are pulled into the invading water.

The wettability of particles can induce interfacial instabilities in the otherwise viscously stable regime at $M < 1$. The injection of water into a Hele–Shaw cell filled with dry, partially

Poiseuille number:
balance between force
density and viscosity;

$$N_{\Psi\eta} \equiv \frac{\Psi d^2}{\eta v}$$

wettable particles induces fingering of the water–air interface at low capillary numbers (Bihi et al. 2016). The water–air interface initially expands radially with particles collecting on it, as water preferentially wets the particles. Upon reaching a critical radius, the interface begins to form fingers, creating more surface area for particles to adsorb onto, thereby lowering the total interfacial energy (see image in **Figure 3c**).

3.4. Transition to a Porous Medium: Fracturing

The previous discussions involve granular media that are relatively mobile far below the jamming limit, except for the highly localized compaction layer near the fluid–fluid interface. When the initial particle volume fraction is close to ϕ_m , the granular suspension effectively behaves like a porous medium with an interstitial fluid. This transition of the granular material from a fluid-like to a solid-like state sets the onset of fluid invasion via fracturing (Sandnes et al. 2011), which is distinct from fingering. As exemplified in **Figure 3d, subpanel iii**, fracturing is often characterized by “thin fingers with long, straight segments,” distinct from rounded fingers that are dominated by capillarity or viscosity (Holtzman et al. 2012, p. 2). When ϕ is further increased to the jamming limit, particles are effectively immobile, and air invades the pore space between the particles by expelling the interstitial fluid.

In the case of air invading a shear-thickening cornstarch suspension, a transition from viscous fingering to fracturing occurs as the suspension reaches a discontinuous shear-thickening state upon an increase in ϕ (Ozturk et al. 2020). The discontinuous shear-thickening behavior stems from the particles establishing a network of frictional contacts. When only the invasion front is in the discontinuous shear-thickening state, fracturing remains localized, termed dendritic fracturing. In this regime, the cornstarch suspension relaxes back to a liquid-like state once the fracturing front has passed by. In contrast, when ϕ is further increased toward the unstressed jamming limit, the suspension becomes shear jammed, which leads to system-wide fracturing, as shown in **Figure 3d, subpanel vi**.

4. ONE IN MANY: FLOWS GOVERNED BY VISCOSITY AND FORCE DENSITY

In the previous section, we saw how fluid invasion into a particulate suspension leads to distinct regimes within a single flow geometry, depending on the dominant mechanical quantities. Here, we highlight how suspension flows and their instabilities can be governed by the same mechanical balance across diverse geometries. As an example, we consider the interplay between viscosity η and force density Ψ . The dimensionless number associated with this pair of mechanical quantities can be expressed in the traditional hydrodynamic form using a characteristic velocity v and length scale ℓ . This balance classically appears in Hagen–Poiseuille flows, where $\Psi D^2/(\eta v) \propto 1$, leading to parabolic velocity profiles with $v \propto (\Psi/\eta)D^2$, where D represents a coordinate perpendicular to the flow direction, often the radius of a pipe (Batchelor 2000). The dimensionless number is referred to as the Poiseuille number (Catchpole & Fulford 1966), and we denote it as $N_{\Psi\eta}$ when it is defined using the particle size d . The force density can be understood as a pressure gradient $\Psi \propto \Sigma/\ell$, which for gravity-driven flows simplifies to $\Psi \propto \rho g$. Remarkably, this same dimensionless number appears in phenomena far beyond this classical origin.

4.1. Sediment Transport

Sediment flow refers to the motion of solid particles suspended in a fluid, typically driven by gravity, pressure gradients, or shear forces. These flows are common in rivers, coastal environments, and underwater avalanches, and they are prone to instabilities (Pächt et al. 2020,

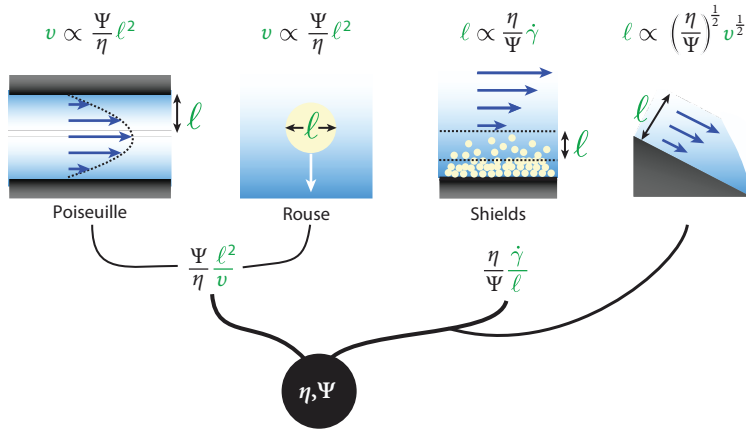


Figure 4

Three similar dimensionless numbers defined from the combination of a viscosity η and a force density Ψ . The force density is usually a weight density, i.e., $\Psi = \rho g$, but may also be a pressure gradient, $\Psi = \Sigma/\ell$, in particular in the context of Poiseuille flows.

Minier et al. 2023). Key examples are turbidity currents, where suspended particles increase the density of the fluid, driving a self-sustaining, gravity-driven flow (Meiburg & Kneller 2010), or the Rayleigh–Taylor instability that occurs as a denser sediment-laden fluid lies above a less-dense fluid and leads to finger-like intrusions (Burns & Meiburg 2015, Kobayashi & Kurita 2022, Guo et al. 2024). Shear-driven instabilities such as the Kelvin–Helmholtz instability can also develop at the interface between layers that move at different velocities, causing sediment waves or roll structures (Nesterov 2022). Dune and ripple formation results from sediment transport driven by a fluid shear stress, leading to complex bedform patterns (Mazumder 2003).

In the context of the initiation of motion of sediments in fluid flows, the inverse of the Poiseuille number $N_{\Psi\eta}$ is closely related to the Shields number (Shields 1936) (**Figure 4**), which in its general form involves an unspecified stress Σ :

$$\text{Sh} \equiv \frac{\Sigma}{\Psi d}, \quad 9.$$

where d is the particle size and $\Psi = (\rho_p - \rho_f)g$ represents the effective force density of a suspension with particle density ρ_p and liquid density ρ_f .

If the stress is a viscous stress, $\Sigma \propto \eta\dot{\gamma}$, then $\text{Sh} = \eta\dot{\gamma}/(\Psi d) \propto N_{\Psi\eta}^{-1}$, corresponding to the viscous Shields number, where the shear rate can be expressed from a velocity gradient. This formulation is relevant for studying the resuspension of a particle bed by a viscous shear flow above (Charru & Mouilleron-Arnauld 2002, Charru & Hinch 2006, Aussillous et al. 2013, Valance & Berzi 2022). The flow induces a mobile sediment layer above the bed, with a characteristic thickness $\ell \propto \eta\dot{\gamma}/\Psi$, leading to $N_{\Psi\eta} \propto d/\ell$. A prefactor β , dependent on the initial packing fraction of the bed, ϕ , refines the relationship, such that $N_{\Psi\eta} = \beta d/\ell$ (Charru & Mouilleron-Arnauld 2002).

If the stress is an inertial stress, $\Sigma \propto \rho v^2$, then $\text{Sh} \propto \rho v^2/(\Psi d) \propto v^2/(gd)$, which is equivalent to the Froude number $\text{Sh} = N_{\rho\Psi}$, where v is a flow velocity over the sediment bed. Depending on the values of the Shields and Reynolds numbers, a variety of patterns can form, from ripples and dunes at the surface of the sediments to turbulent resuspension (Shields 1936, van Rijn 1984, Charru et al. 2013, Pätz et al. 2020, Ancy & Recking 2023, Minier et al. 2023).

In the case where the stress is independent of kinematics, for instance, if it has rheological origins as an elastic modulus or a yield stress, then we have $\text{Sh} = N_{\Sigma\Psi}^{-1}$. This number is useful in

studying sedimentation in viscoelastic or yield stress fluids (Abedijaberi & Khomami 2012, Padhy et al. 2013, Whorton et al. 2025) or flows over viscoelastic muds (Dade et al. 1992, Behera et al. 2018, van Rijn 2020).

4.2. Bubbles in Suspensions

Bubbles in particulate suspensions play an important role in various natural and industrial processes, including flotation, mixing, and transport phenomena. Their behavior is influenced by particle concentration, size distribution, and the physicochemical properties of the surrounding fluid. Particles can attach to bubbles, altering their rise velocity and stability, which is essential in applications including mineral flotation and wastewater treatment (Ahmed & Jameson 1985, Verrelli et al. 2011, Lohse 2018, Yu et al. 2018, Wang & Liu 2021).

The shape and motion of bubbles can again be rationalized considering the Poiseuille number $N_{\Psi\eta}$, expressed as the ratio of hydrostatic stress to viscous stress, $(\Psi d)/(\eta v/d)$, or alternatively as a ratio of velocities:

$$N_{\Psi\eta} \equiv \frac{\Psi d^2}{\eta v} \propto \frac{v_s}{v}, \quad 10.$$

where $v_s \equiv (\Psi/\eta)d^2$ is the settling velocity of a particle of size d . In this form, the Poiseuille number is also known as the Rouse number, as shown in **Figure 4** (Andreotti & Claudin 2013).

When viscosity dominates, Stokes's solution for the rising velocity of a bubble of density ρ_b and diameter d in a fluid of density ρ_f and viscosity η is $v_s \equiv g(\rho_b - \rho_f)d^2/(18\eta)$, which can be written more succinctly as $v_s \propto (\Psi/\eta)d^2$. If v is the rising velocity of the bubble, Stokes's solution corresponds to $v/v_s \propto 1$, implying $N_{\Psi\eta} \propto 1$. However, if additional mechanical effects come into play, the actual velocity v may substantially deviate from v_s , and in extreme cases, a bubble may stop rising altogether.

A recent study (Lilin et al. 2024a) illustrates this by investigating air injection from a nozzle at the bottom of a three-dimensional cornstarch suspension. The volumetric flow rate is controlled via gauge pressure, and the volume fraction ϕ of the suspension is varied. Two distinct scenarios emerge, as shown in **Figure 5a**. At low flow rates and moderate ϕ , the injected air forms a bubble that detaches from the nozzle and rises in the suspension. At higher flow rates or larger ϕ , the air fractures the suspension, forming an irregular cavity that remains attached to the nozzle.

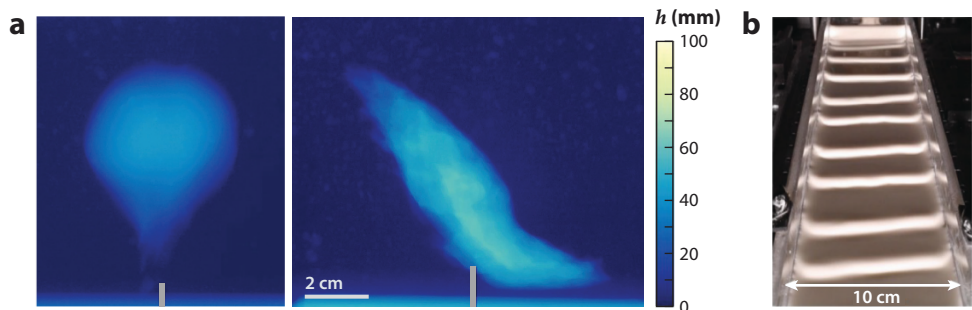


Figure 5

(a) Air injection into a dense cornstarch suspension exhibits a transition from bubbles to fractures at the onset of discontinuous shear thickening. Pressurized air is injected from a nozzle placed at the bottom of a three-dimensional container filled with a dense cornstarch suspension. The color bar denotes the thickness h of the air cavity. Panel adapted from Lilin et al. (2024a) (CC BY 4.0). (b) Oobleck waves emerging as a dense cornstarch suspension flows down an incline. Panel adapted from Darbois Texier et al. (2020) (CC BY 4.0).

Bubbles that rise do so according to Stokes's solution, $N_{\Psi\eta} \propto 1$. The cavities that remain attached to the nozzle, instead, grow in size as long as air is injected, and their center rises at a velocity $v_g \propto R/t$, where $R(t)$ is the time-dependent bubble radius. If $v_s \gtrsim v_g$, the bubble might eventually detach, which can be expressed using a Poiseuille-like number as $\eta/(\Psi R t) \lesssim 1$. However, this should not be confused with $N_{\Psi\eta} \equiv \eta v/(\Psi d^2)$, as the two numbers are equivalent only when $v \propto R/t$. During cavity formation, the cavity surface exhibits an irregular fractured profile due to the shear-thickening nature of the suspension. To facilitate comparison with the dynamics of bubbles in other non-Newtonian fluids, we may use the minimum viscosity before the onset of discontinuous shear thickening, η_0 , to define the stress denoting the onset of discontinuous shear thickening $\Sigma_c \equiv \eta_0 \dot{\gamma}_c$, where $\dot{\gamma}_c$ is the shear rate at the onset of discontinuous shear thickening. For cornstarch suspensions, Σ_c is a few pascals and roughly independent of ϕ . This stress scale Σ_c needs to be considered in the description of fracturing cavities, in addition to the force density Ψ and the viscosity η . This trio of mechanical quantities has an associated length scale $\ell_{\Sigma\Psi} \propto \Sigma_c/\Psi$. Assuming $\Sigma_c \simeq 1\text{--}10$ Pa would yield a length scale of the order 0.1 to 1 mm, potentially indicating a lower bound for the cavity size at the onset of fracture.

4.3. Suspension Flow Down an Incline

The combination of viscosity and force density also plays a key role in flows down an incline. Depending on the particle concentration, density, or size distribution, suspensions can exhibit various flow regimes, including uniform settling, stratification, and the formation of waves (Chang 1994, Snabre 2000, Winterwerp 2006). When viscosity dominates over inertia, the height of the fluid film, D , is given by

$$D \propto \left(\frac{\eta v}{\Psi}\right)^{\frac{1}{2}} \leftrightarrow N_{\eta\Psi} \propto N_0^2, \quad 11.$$

where v is the characteristic velocity of the fluid film. The force density $\Psi \equiv \rho g \sin \theta$ accounts for the slope θ of the incline.

For a higher film velocity v , inertia has an impact. Unstable surface undulations associated with roll waves inside the fluid emerge (Chang 1994). The onset of this so-called Kapitza instability is typically expressed in terms of a Reynolds number, $\rho v D/\eta > (5/4) \cot \theta$ (Liu et al. 1993). Using Equation 12, this criterion can be rewritten as a macroscopic Froude number $\rho v D/\eta \propto \rho v^2/(\Psi D)$ (Balmforth & Mandre 2004) and the instability threshold as $4\rho v^2/(5\rho g \cos \theta D) > 1$. All together, this can be summarized as $N_0 N_{\rho\Psi} \gtrsim 1$ with an appropriately defined force density. This highlights the importance of three dimensionless numbers in describing the onset of the Kapitza instability: the Froude number $N_{\rho\Psi}$, the Reynolds number $N_{\rho\eta}$, and the Poiseuille number $N_{\eta\Psi}$.

The phenomenology of the Kapitza instability was first developed for Newtonian fluids, but similar roll waves emerge in non-Newtonian fluids, including in particulate suspensions (Coussot 1994; Forterre & Pouliquen 2003; Balmforth & Liu 2004; Balmforth et al. 2005; Tamburrino & Ihle 2013; Mounkaila et al. 2021, 2023; Balmforth 2025). A recent example involves a dense cornstarch suspension flowing down an incline, as shown in **Figure 5b** (Darbois Texier et al. 2020, 2023). The nature of the instability depends on the volume fraction ϕ of cornstarch in water. For low volume fractions, the instability threshold remains comparable to that of Newtonian fluids, i.e., $N_0^{-1} N_{\rho\eta} \gtrsim 1$ or equivalently $N_0 N_{\rho\Psi} \gtrsim 1$. For volume fractions above approximately 0.42, however, the critical macroscopic Froude (or Reynolds) number denoting the onset of the instability drops sharply, reaching values as low as $N_0 N_{\rho\Psi} \gtrsim 0.01$ for $\phi \simeq 0.5$. This suggests that inertia is no longer the driving factor. As we see in Section 5.4, these observations can be rationalized by considering the shear-thickening nature of the suspension.

Morton number:
 surface tension,
 density, viscosity, and
 force density;
 $N_{\Psi\eta\rho\Gamma} \equiv \frac{\Psi\eta^4}{\Gamma^3\rho^2}$

When density, viscosity, force density, and surface tension Γ are considered together, a single dimensionless number can be built, the Morton number, $N_{\rho\eta\Gamma\Psi} \equiv \Psi\eta^4/(\Gamma^3\rho^2)$. In the context of flows down inclines, the related Kapitza number is often used, defined as $N_{\rho\eta\Gamma\Psi}^{-\frac{1}{3}}$ (Chang 1994). Most experiments and analyses of the Kapitza instability and its nonlinear development have focused on the small Morton number regime (i.e., high Kapitza numbers), as is the case for water, where typically $N_{\rho\eta\Gamma\Psi} \simeq 3 \times 10^{-11}$ (Mendez et al. 2017). Interestingly, for cornstarch suspensions, the value of $N_{\rho\eta\Gamma\Psi}$ depends on the volume fraction ϕ , due to the strong dependence of the suspension viscosity on ϕ (Darbois Texier et al. 2020, 2023). Rheological measurements reported by the authors indicate that $N_{\rho\eta\Gamma\Psi} \simeq 1$ (assuming $\Gamma = 10^{-2}$ N/m) at the critical volume fraction ϕ_c for discontinuous shear thickening, and that for $\phi > \phi_c$ we have $N_{\rho\eta\Gamma\Psi} > 1$. It would be interesting to investigate whether this change in the Morton number regime plays a role in the surface waves observed in cornstarch suspensions (Balmforth et al. 2005, Darbois Texier et al. 2020, 2023).

4.4. Fluid Invasion

As a final example highlighting the interplay between viscosity and force density, we return to the fluid invasion experiments reviewed in Section 3, where $N_{\Psi\eta}$ appears under yet another name as the frictional dimensionless number (Dumazer et al. 2020).

In experiments on capillary bulldozing of granular beds in a quasi-one-dimensional geometrical confinement, a state diagram distinguishing two regimes—viscous and frictional—observed by varying the volumetric flow rate q and the particle size d , is established (Dumazer et al. 2016, 2020). The transition between the two regimes is characterized by a frictional dimensionless number, expressed as a ratio of stresses:

$$N \equiv \frac{\Sigma_{\text{visc}}}{\Sigma_{\text{fric}}} \equiv \frac{\frac{\eta}{k_0} \frac{4q}{\pi D^2} \ell}{(\Sigma_0 + \Sigma_g/\kappa) \exp(\ell/\lambda) - \Sigma_g/\kappa}. \quad 12.$$

How can this complex expression be related to something as simple as the Poiseuille number? The numerator represents the viscous stress derived from Darcy's law, where D is the diameter of the confining tube, ℓ is the characteristic size of the particle accumulation front, and k_0 is the permeability. The denominator represents the frictional stress given by Janssen's law (Janssen 1895), where Σ_0 is the longitudinal stress boundary condition and $\Sigma_g \equiv \phi_m \Delta\rho g D/4$ is the hydrostatic stress due to the density difference between the particles and the liquid $\Delta\rho$, with ϕ_m the maximal packing fraction. The friction length is given by $\lambda \equiv D/(4\mu\kappa)$, where $\mu \simeq \Sigma_0/\Sigma_g$ is a friction coefficient and κ is the Janssen coefficient.

While the expression for the frictional number in Equation 12 is remarkable for its thoroughness, the many parameters obscure its essence. Experiments suggest that one can consider $\kappa = 0.7$ and $\mu = 0.1$ (Dumazer et al. 2020). Neglecting numerical factors of the order 1, we find $\lambda \propto D$, and the accumulation front similarly scales as $\ell \simeq D$ (Dumazer et al. 2020). The exponential term in Equation 12 then reduces to a quantity of the order 1, and the denominator simplifies to $\Sigma_0 \propto \Sigma_g \propto \Psi D$. In addition, the permeability follows the relation $k_0 \propto d^2$, and the flow rate can be expressed as $q \propto v D^2$. With these simplifications, Equation 12 reduces to

$$N \propto \frac{\frac{\eta}{d^2} \frac{v}{D^2} D}{\Psi D} \propto \frac{\eta v}{\Psi d^2} \propto N_{\Psi\eta}^{-1}. \quad 13.$$

This reveals that the frictional number is essentially the inverse of the Poiseuille number with a characteristic length scale set by the particle size d . When it is expressed in this form, we believe that analogies with other fields involving the interplay of viscosity and force density are more easily drawn.

5. INTERPLAY BETWEEN NONLINEAR RHEOLOGY AND PATTERN GROWTH

One of the reasons particle suspensions exhibit such a striking diversity of patterns is that their rheology can evolve dynamically during the pattern growth. When driven out of equilibrium, either by a flow or when exposed to drying, the rheology of the suspension may change. This can induce instabilities in situations where a pure liquid would remain stable, leading to particularly stunning effects if the suspension transitions dynamically from a fluid-like to a solid-like state. These transitions also challenge the traditional approach to analyzing instabilities in terms of dimensionless numbers based on fixed material properties. For instance, if dimensionless numbers such as a Reynolds number $N_{\eta\rho}$, a capillary number $N_{\eta\Gamma}$, or a Weissenberg number $N_{\eta\Sigma}$ are defined using a viscosity η , then any flow-induced changes in viscosity must be taken into account.

5.1. Instabilities Favored by Spatial Gradients in Viscosity

A notable example of the nontrivial effects that can occur dynamically in suspension flows is the invasion of a suspension in a radial Hele–Shaw cell (Tang et al. 2000, Xu et al. 2016, Kim et al. 2017, Luo et al. 2018, Hooshanginejad et al. 2019, Xu & Lee 2019). The more viscous suspension displaces less viscous air, implying an unfavorable viscosity contrast for the emergence of viscous-fingering instabilities such that the interface is expected to remain stable. Counterintuitively, though, after a certain time, the interface develops undulations that grow into fingers, as shown in **Figure 6a**. The instability arises from the shear-induced migration of the particles (Leighton & Acrivos 1987a,b; Phillips et al. 1992) that forces the particles to the centerline where the velocity is higher than the mean flow velocity. This effect guides the particles toward the liquid–air interface, where they accumulate in a band. The viscosity in the band is increased as a result of this accumulation of particles, which induces a destabilizing viscosity gradient that causes the fingering instability. Particle accumulation tends to be sharper and less gradual as the particle size becomes large compared to the plate spacing ($N_0 \rightarrow 1$) (Kim et al. 2017, Chen et al. 2021), which in turn causes the instability to become more pronounced with the formation of large particle clusters.

A similar phenomenon occurs even in the absence of a liquid–air interface, when the suspension and the displaced less-viscous fluid are density mismatched (Kudrolli et al. 2020). The sedimentation of the particles leads to the formation of a particle-rich front even for small density differences. This front generates a local viscosity gradient that enables fingering instabilities to emerge. The timescale over which the instability develops is governed by the settling time of the particles in the cell, which can be tuned by controlling the volume fraction of particles.

5.2. Dynamic Liquid-to-Solid Transition Induces Cracks

As discussed in Section 3.4, a dynamic increase in the particle volume fraction during fluid invasion into a suspension can lead to either gap-spanning frictional contacts or jamming, which dramatically modifies the resulting patterns. This compactification of the particles pushes the material toward a threshold beyond which it transitions to a solid-like behavior, causing fracture-like pattern growth (Sandnes et al. 2011; Eriksen et al. 2018; Olsen et al. 2019; Meng et al. 2020, 2022; Flekkøy et al. 2023). This implies a stress buildup in the compactified region, which eventually becomes larger than the energetic cost of creating fractures.

Such stress buildup in suspensions is not limited to compactification by fluid invasion. It also occurs spontaneously as an aqueous suspension dries. This process is classically studied by letting a drop of an aqueous particle suspension evaporate on a substrate (Routh 2013, Goehring & Morris 2014, Goehring et al. 2015). It leads to a stunning richness of phenomena

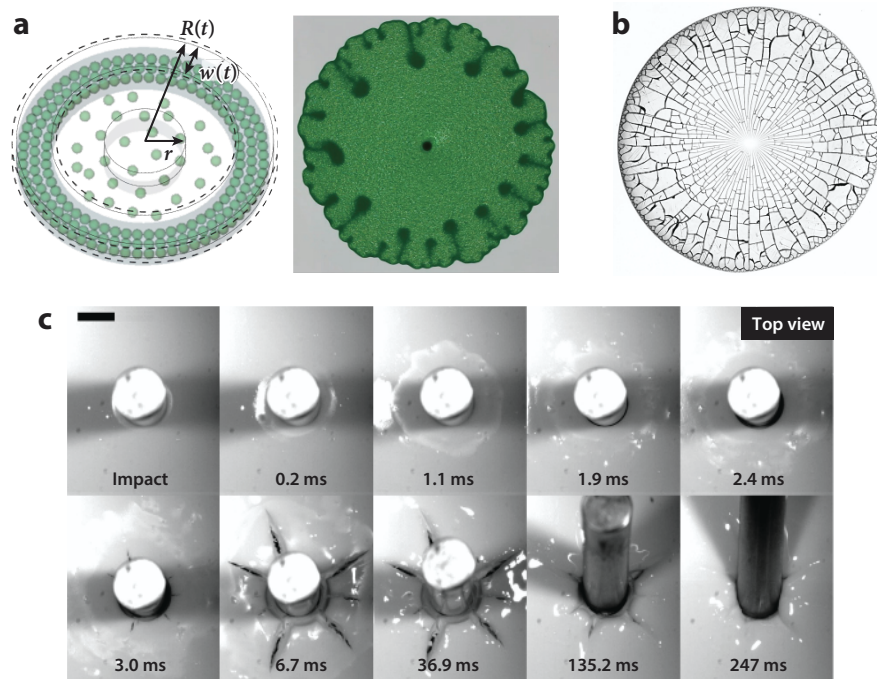


Figure 6

(*a*) Shear-induced migration brings particles (*green*) to the interface. This leads to a shear-induced spatial gradient in viscosity that induces fingering instabilities. Panel adapted from Kim et al. (2017). (*b*) Stress buildup during evaporation of a suspension drop induces an intricate crack pattern in the particle deposit. Panel adapted from Lilin et al. (2024b) (CC BY 4.0). (*c*) Impact of a projectile onto a dense cornstarch suspension solidifies the material and leads to crack formation. Panel adapted with permission from Roché et al. (2013).

depending on the contact angle between the drop and the substrate, the initial particle volume fraction, or the stiffness and size of the particles (Giorgiutti-Dauphiné & Pauchard 2014). On a hydrophilic substrate, the contact line of the drop remains pinned to the substrate, which induces a capillary-driven flow that transports particles to the edge of the drop, where they assemble into a solid-like deposit. At a low particle volume fraction, this results in the famous coffee-ring effect (Deegan et al. 1997). At a higher particle volume fraction, the deposit extends across the entire initially wetted area (Bourriane et al. 2021, Lilin & Bischofberger 2022). Stresses build up in the deposit that are eventually released by forming fractures, inducing intricate—and stunningly beautiful—crack patterns, as shown in **Figure 6b** (Lilin et al. 2024b). For suspension drops drying on hydrophobic substrates, it has recently been shown that two distinct solid-like instabilities can occur sequentially: a shape instability in the form of air invagination, followed by a cracking instability (Milani et al. 2023). As water evaporates, a particle-rich shell forms at the liquid–air interface. Over time, this shell densifies and eventually reaches a glassy (repulsive, unaggregated) state, which triggers the first shape instability and air invasion. Sudden macroscopic fracture occurs at a later stage when the particles irreversibly aggregate.

5.3. Complex Rheology of Dense Suspensions Induces Fracturing

A class of materials that exhibits a striking response to an applied shear rate or stress is dense suspensions—as anyone who has played with a suspension of cornstarch in water can attest. Dense

suspensions exhibit the ability to switch dynamically and reversibly from a fluid-like to a solid-like state (Morris 2020). At a high enough concentration of particles, the suspension exhibits discontinuous shear thickening, where the suspension viscosity increases by several orders of magnitude as a critical shear rate is reached. The onset of such discontinuous shear thickening occurs as the particle interactions transition from lubricated to frictional contacts. The frictional contacts lower the critical particle volume fraction at which the system jams compared to the stress-free lubricated case. If the stress applied to the suspension is increased further, the suspension can enter a solid-like, shear-jammed state (Peters et al. 2016).

These rheological transitions manifest themselves in spectacular ways in emerging patterns inside dense suspensions. In experiments performed in the confinement of a Hele–Shaw cell, they induce transitions from fingering-like invasion of air into the suspension to invasion by fracturing the material (Ozturk et al. 2020). Air injection into a three-dimensional bulk dense suspension can lead to either smooth bubbles or sharp fractures, depending on the volume fraction of the suspension and the applied pressure (Lilin et al. 2024a). The fractures can subsequently relax to bubbles that then rise under buoyancy. The onset of relaxation occurs as the shear rate induced by the growth of the air cavity decreases below the critical shear rate denoting the onset of discontinuous shear thickening, which reveals a structural signature of the shear-jammed state. Another manifestation of such a dynamic liquid-to-solid transition is the fracturing behavior of thin layers of suspensions upon the impact of a projectile (Roché et al. 2013), illustrated in **Figure 6c**. The stress from the impact solidifies the material, opening a hole around the impacting rod. Cracks then emerge on the contour of the hole and propagate outward, accompanied by plastic flow.

Finally, the dynamic change in the suspension rheology with shear rate leads to a new type of instability in flows down an incline, as discussed in the context of relevant dimensionless numbers in Section 4.3. A transition from the traditional Kapitza waves to a wave-like instability of fundamentally different nature, termed Oobleck waves, occurs at the volume fraction that denotes the onset of discontinuous shear-thickening behavior (Balmforth et al. 2005; Darbois Texier et al. 2020, 2023). These Oobleck waves emerge at a very low Froude number, implying that they are a noninertial instability specific to free-surface flows. At the heart of the growth of the Oobleck waves is the rheology of the suspension in the discontinuous shear-thickening state, which is characterized by an S-shaped curve of the shear stress Σ versus the shear rate $\dot{\gamma}$. If a perturbation in the height of the suspension layer spontaneously occurs, a force balance on the material requires that the basal stress upstream of the perturbation decreases, while that downstream of the perturbation increases. Owing to the S-shaped rheology of the suspension, when $d\dot{\gamma}/d\Sigma < 0$, a decrease in the stress requires a local increase in the shear rate and vice versa. The shear rate thus increases upstream and decreases downstream of the perturbation, leading to an amplification of the initial perturbation and the growth of the Oobleck waves.

5.4. Impact of Aging on Instabilities in Attractive Suspensions

Introducing attractive interactions between the particles leads to a liquid-to-solid transition due to the formation of a three-dimensional percolated network. The resulting soft solid displays time-dependent mechanical properties referred to as aging. Such an evolution is prompted by the gradual rearrangement and restructuring of the sample microstructure, yielding a progressive increase in the material's elasticity, which directly impacts the interfacial instabilities that develop when the fluid is displaced, as recently illustrated in suspensions of attractive clay particles (Palak et al. 2022, 2023; Parmar & Bandyopadhyay 2024).

At short aging times, when the suspension is still predominantly fluid-like, displacement results in dense, viscous patterns characterized by closely spaced, highly branched fingers that undergo

STRIPE PATTERNS IN SHEARED SUSPENSIONS OF ATTRACTIVE PARTICLES

Suspensions of attractive particles exhibit a complex response to shear, often leading to flow instabilities and spatial structuring. A striking example is the formation of log-rolling flocs, where attractive particles suspended in a Newtonian liquid spontaneously self-organize into structures aligned along the vorticity direction, creating a distinctive striped pattern (**Figure 1a,b**). This phenomenon occurs exclusively when the suspension is sheared within a confined geometry at sufficiently low shear rates. It is observed in a wide range of suspensions, including attractive emulsions; colloid–polymer mixtures; and suspensions of carbon black, carbon nanotubes, and graphene oxide (Lin-Gibson et al. 2004, Montesi et al. 2004, Grenard et al. 2011, Godfrin et al. 2013). The formation of these log-like structures arises from the hydrodynamic coupling between particle-rich flocs and the confining boundaries (Varga et al. 2019). Clusters of particles, driven together by attractive forces, generate periodically spaced viscous eddies that act as stable regions for further particle aggregation. The stability of the log-rolling flocs is characterized by the Mason number that quantifies the balance between shear forces and interparticle attraction.

frequent tip splitting and merging. As the suspension continues to age and its elasticity increases, the instability shifts to patterns with well-defined primary branches and more regular and distinct secondary side branches. In strongly aged suspensions, the material becomes more solid-like, leading to viscoelastic fracturing where cracks propagate in a brittle-like manner characterized by sharp, elongated primary fractures and perpendicular secondary offshoots. This transition occurs when the internal stresses accumulated in the material exceed the energy required for fracture propagation. These findings highlight the critical role of aging in determining whether fluid displacement results in smooth deformations or fracture-dominated growth.

Additionally, at a fixed sample age, the flow rate of the displacing fluid also affects the pattern, which transitions from viscoelastic fractures to branched fingers as the flow rate increases. This observation suggests that pattern formation in aging suspensions could be described in a unified framework encompassing the strength of interparticle attractive forces and the strength of the flow. The competition between these two factors is captured by the Mason number $N_{F\eta} \equiv \eta d^2 \dot{\gamma} / F$, where η denotes the viscosity of the suspending fluid, F is the attractive interparticle force, and $\dot{\gamma}$ is the shear rate (Varga & Swan 2018). Within this framework, displacement at a high flow rate or short aging times corresponds to $N_{F\eta} \gtrsim 1$ and fully disrupts the gel structure, promoting a liquid-like response of the material. In contrast, displacements at $N_{F\eta} \lesssim 1$ result in a dynamic yielding as bulk pieces of gel slip past each other, favoring the growth of cracks. In the latter case, if the gel sample is sheared instead of being displaced, the coupling with hydrodynamic forces induces the formation of log-rolling flocs whose stability is also understood in terms of the Mason number (Varga et al. 2019), as discussed in the sidebar titled *Stripe Patterns in Sheared Suspensions of Attractive Particles*.

6. CONCLUSIONS

In this journey through pattern growth in particulate suspensions, we have highlighted how the inclusion of particles in a fluid can unlock novel instabilities and flow phenomena due to spatial confinement, frictional interactions, or dynamic rheological transitions. The complexity of the landscape leaves vast opportunities for further discoveries, both in exploring limits of regimes and in revealing transitions between regimes dominated by distinct mechanical quantities. This motivates continued experimental explorations and approaches that can bring some order and sense into the extensive existing data. We hope that our framework for constructing dimensionless numbers from mechanical considerations can contribute to this endeavor.

Deciphering the underlying mechanisms of suspension flows and their instabilities not only satisfies curiosity, but it might allow for exploiting patterning to design materials. The patterns could be leveraged in the development of advanced composite materials, where the alignment and distribution of particles govern the mechanical strength, electrical conductivity, or thermal properties of the material. Additionally, shear-induced patterning can be applied in the design of coatings, sensors, and membranes, where the creation of specific surface textures or porosities is crucial for functionality. Many of the phenomena discussed in this review are largely scale invariant, and instabilities probed in the laboratory reveal mechanisms at play in ocean sediments, river networks, or desert mud. A fascinating ongoing process is to deepen the connections between phenomena discussed in this review and geophysical processes (Cartwright et al. 2024).

SUMMARY POINTS

1. The interplay between viscous, inertial, and frictional effects in particulate suspensions leads to a uniquely rich nonequilibrium behavior in suspension flows.
2. Shear-induced migration, particle compactification, or shear-driven particle contact networks can induce dynamic transitions from a liquid-like to a solid-like state. This can give rise to suspension fracturing or to friction-dominated intermittent growth dynamics.
3. Instabilities involve at least two mechanical factors: one playing the role of a driving force, the other that of a resisting force. These colloquial forces can stem from a host of mechanical quantities; we here highlight viscosity, density, force density, surface tension, and a measure of stress.
4. A plethora of dimensionless numbers is used in the literature, with nomenclature that varies within communities and according to usage. Standardizing these dimensionless numbers could provide a more universal framework that can enable analogies to be drawn across diverse areas of suspension physics. This framework can help identify relevant dimensionless numbers and their relationships. While the Buckingham π theorem states how many dimensionless numbers are required, the framework helps rationalize how to select them.

DISCLOSURE STATEMENT

The authors are not aware of any affiliations, memberships, funding, or financial holdings that might be perceived as affecting the objectivity of this review.

ACKNOWLEDGMENTS

T.D. acknowledges support from the National Science Foundation (NSF) (grant PHY-2309135 to the Kavli Institute for Theoretical Physics). S.L. acknowledges support from the NSF (grants DMR-2003706 and EAR-2100493). I.B. acknowledges support from the American Chemical Society Petroleum Research Fund (grant 66034-ND9).

LITERATURE CITED

- Abedijaberi A, Khomami B. 2012. Sedimentation of a sphere in a viscoelastic fluid: a multiscale simulation approach. *J. Fluid Mech.* 694:78–99
- Ahmed N, Jameson GJ. 1985. The effect of bubble size on the rate of flotation of fine particles. *Int. J. Miner. Process.* 14:195–215

- Ancey C, Recking A. 2023. Scaling behavior of bedload transport: What if Bagnold was right? *Earth-Sci. Rev.* 246:104571
- Andreotti B, Claudin P. 2013. Aeolian and subaqueous bedforms in shear flows. *Philos. Trans. R. Soc. A* 371:20120364
- Aussillous P, Chauchat J, Pailha M, Médale M, Guazzelli E. 2013. Investigation of the mobile granular layer in bedload transport by laminar shearing flows. *J. Fluid Mech.* 736:594–615
- Bagnold RA. 1954. Experiments on a gravity-free dispersion of large solid spheres in a Newtonian fluid under shear. *Proc. R. Soc. A* 225:49–63
- Balmforth NJ. 2025. Instability of falling films of discontinuously shear-thickening fluid. *J. Fluid Mech.* 1002:A34
- Balmforth NJ, Bush JWM, Craster RV. 2005. Roll waves on flowing cornstarch suspensions. *Phys. Lett. A* 338(6):479–84
- Balmforth NJ, Liu JJ. 2004. Roll waves in mud. *J. Fluid Mech.* 519:33–54
- Balmforth NJ, Mandre S. 2004. Dynamics of roll waves. *J. Fluid Mech.* 514:1–33
- Barral Q, Ovarlez G, Chateau X, Boujlel J, Rabideau B, Coussot P. 2010. Adhesion of yield stress fluids. *Soft Matter* 6(6):1343–51
- Batchelor GK. 2000. *An Introduction to Fluid Dynamics*. Cambridge University Press
- Burns P, Meiburg E. 2015. Sediment-laden fresh water above salt water: nonlinear simulations. *J. Fluid Mech.* 762:156–95
- Behera H, Das S, Sahoo T. 2018. Wave propagation through mangrove forests in the presence of a viscoelastic bed. *Wave Motion* 78:162–75
- Bihi I, Baudoin M, Butler JE, Faille C, Zoueshtiagh F. 2016. Inverse Saffman–Taylor experiments with particles lead to capillarity-driven fingering instabilities. *Phys. Rev. Lett.* 117(3):034501
- Bischofberger I, Ramachandran R, Nagel SR. 2014. Fingering versus stability in the limit of zero interfacial tension. *Nat. Commun.* 5:5265
- Bourrianne P, Lilin P, Sintès G, Nirca T, McKinley GH, Bischofberger I. 2021. Crack morphologies in drying suspension drops. *Soft Matter* 17:8832–37
- Cartwright JH, Cockell CS, Goehring L, Holler S, Jordan SF, et al. 2024. Self-organized pattern formation in geological soft matter. Preprint, arXiv:2412.18999v1 [physics.geo-ph]
- Catchpole JP, Fulford G. 1966. Dimensionless groups. *Ind. Eng. Chem.* 58(3):46–60
- Chang HC. 1994. Wave evolution on a falling film. *Annu. Rev. Fluid Mech.* 26:103–36
- Charru F, Andreotti B, Claudin P. 2013. Sand ripples and dunes. *Annu. Rev. Fluid Mech.* 45:469–93
- Charru F, Hinch EJ. 2006. Ripple formation on a particle bed sheared by a viscous liquid. Part 1. Steady flow. *J. Fluid Mech.* 550:111–21
- Charru F, Mouilleron-Arnould H. 2002. Instability of a bed of particles sheared by a viscous flow. *J. Fluid Mech.* 452:303–23
- Chen Y, Luo R, Wang L, Lee S. 2021. Self-similarity in particle accumulation on the advancing meniscus. *J. Fluid Mech.* 925:A10
- Chevalier C, Lindner A, Clement E. 2007. Destabilization of a Saffman–Taylor fingerlike pattern in a granular suspension. *Phys. Rev. Lett.* 99:174501
- Coussot P. 1994. Steady, laminar flow of concentrated mud suspensions in open channels. *J. Hydraul. Res.* 32(4):535–59
- Dade WB, Nowell ARM, Jumars PA. 1992. Predicting erosion resistance of muds. *Mar. Geol.* 105(1–4):285–97
- Darbois Texier B, Lhuissier H, Forterre Y, Metzger B. 2020. Surface-wave instability without inertia in shear-thickening suspensions. *Commun. Phys.* 3(1):232
- Darbois Texier B, Lhuissier H, Metzger B, Forterre Y. 2023. Shear-thickening suspensions down inclines: from Kapitza to Oobleck waves. *J. Fluid Mech.* 959:A27
- Deegan RD, Bakajin O, Dupont TF, Huber G, Nagel SR, Witten TA. 1997. Capillary flow as the cause of ring stains from dried liquid drops. *Nature* 389:827–29
- Derks D, Lindner A, Creton C, Bonn D. 2003. Cohesive failure of thin layers of soft model adhesives under tension. *J. Appl. Phys.* 93:1557–66
- Di Vaira NJ, Łaniewski-Wołk Ł, Johnson RL Jr, Aminossadati SM, Leonardi CR. 2022. Influence of particle polydispersity on bulk migration and size segregation in channel flows. *J. Fluid Mech.* 939:A30

- Divoux T, Shukla A, Marsit B, Kaloga Y, Bischofberger I. 2020. Criterion for fingering instabilities in colloidal gels. *Phys. Rev. Lett.* 124:248006
- Dullien FA. 2012. *Porous Media: Fluid Transport and Pore Structure*. Academic Press
- Dumazer G, Sandnes B, Ayaz M, Måløy KJ, Flekkøy EG. 2016. Frictional fluid dynamics and plug formation in multiphase millifluidic flow. *Phys. Rev. Lett.* 117(2):028002
- Dumazer G, Sandnes B, Måløy KJ, Flekkøy EG. 2020. Capillary bulldozing of sedimented granular material confined in a millifluidic tube. *Phys. Rev. Fluids* 5(3):034309
- Eriksen JA, Toussaint R, Måløy KJ, Flekkøy E, Galland O, Sandnes B. 2018. Pattern formation of frictional fingers in a gravitational potential. *Phys. Rev. Fluids* 3(1):013801
- Fardin MA, Hautefeuille M, Sharma V. 2024. Dynamic duos: the building blocks of dimensional mechanics. *Soft Matter* 20:5475–508
- Fardin MA, Perge C, Taberlet N. 2014. “The hydrogen atom of fluid dynamics” – introduction to the Taylor–Couette flow for soft matter scientists. *Soft Matter* 10(20):3523–35
- Flekkøy E, Sandnes B, Måløy K. 2023. Shape of a frictional fluid finger. *Phys. Rev. Fluids* 8:114302
- Forterre Y, Pouliquen O. 2003. Long-surface-wave instability in dense granular flows. *J. Fluid Mech.* 486:21–50
- Giorgiutti-Dauphiné V, Pauchard L. 2014. Elapsed time for crack formation during drying. *Eur. Phys. J. E* 37:39
- Gilbert D, Valette R, Lemaire E. 2022. Impact of particle stiffness on shear-thinning of non-Brownian suspensions. *J. Rheol.* 66:161–76
- Godfrin MP, Hudson SD, Butler PD, Porcar L, Wagner NJ. 2013. Shear-directed assembly of graphene oxide in aqueous dispersions into ordered arrays. *Langmuir* 29:13162–67
- Goehring L, Morris SW. 2014. Cracking mud, freezing dirt, and breaking rocks. *Phys. Today* 67(11):39–44
- Goehring L, Nakahara A, Dutta T, Kitsunezaki S, Tarafdar S. 2015. *Desiccation Cracks and Their Patterns: Formation and Modelling in Science and Nature*. Wiley
- Grenard V, Taberlet N, Manneville S. 2011. Shear-induced structuration of confined carbon black gels: steady-state features of vorticity-aligned flocs. *Soft Matter* 7:3920–28
- Guazzelli É, Pouliquen O. 2018. Rheology of dense granular suspensions. *J. Fluid Mech.* 852:P1
- Guo J, Zhou Q, Zhang Y, Wong RCK. 2024. Experimental investigation of gravitational instabilities at the particle suspension–fluid interface. *Exp. Fluids* 65:43
- Habibi M, Moller P, Fall A, Rafai S, Bonn D. 2012. Pattern formation by dewetting and evaporating sedimenting suspensions. *Soft Matter* 8:4682–86
- Henry C, Minier J-P, Brambilla S. 2023. Particle resuspension: challenges and perspectives for future models. *Phys. Rep.* 1007:1–98
- Holtzman R, Szulczewski M, Juanes R. 2012. Capillary fracturing in granular media. *Phys. Rev. Lett.* 108:264504
- Homsy G. 1987. Viscous fingering in porous media. *Annu. Rev. Fluid Mech.* 19:271–311
- Hooshanginejad A, Druce B, Lee S. 2019. Stability analysis of a particle band on the fluid–fluid interface. *J. Fluid Mech.* 869:R2
- Hoyal DCJD, Bursik MI, Atkinson JF. 1999. Settling-driven convection: a mechanism of sedimentation from stratified fluids. *J. Geophys. Res. Oceans* 104(C4):7953–66
- Janssen HA. 1895. Versuche über getreidedruck in silozellen. *Z. Ver. Dtsch. Ing.* 39:1045
- Kawasaki T, Coslovich D, Ikeda A, Berthier L. 2015. Diverging viscosity and soft granular rheology in non-Brownian suspensions. *Phys. Rev. E* 91:012203
- Kim J, Xu F, Lee S. 2017. Formation and destabilization of the particle band on the fluid–fluid interface. *Phys. Rev. Lett.* 118:074501
- Kobayashi KU, Kurita R. 2022. Key connection between gravitational instability in physical gels and granular media. *Sci. Rep.* 12:6290
- Kozeny J. 1927. Über kapillare Leitung des Wassers im Boden. *Sitz. Akad. Wiss.* 136:271–306
- Kozeny-Carman P. 1937. Fluid flow through granular beds. *Trans. Inst. Chem. Eng.* 15:150–66
- Kudrolli A, Jewel R, Sharma RS, Petroff AP. 2020. Unstable invasion of sedimenting granular suspensions. *Phys. Rev. Lett.* 125(5):054501
- Leighton D, Acrivos A. 1987a. Measurement of shear-induced self-diffusion in concentrated suspensions of spheres. *J. Fluid Mech.* 177:109–31

- Leighton D, Acrivos A. 1987b. The shear-induced migration of particles in concentrated suspensions. *J. Fluid Mech.* 181:415–39
- Lilin P, Bischofberger I. 2022. Criteria for crack formation and air invasion in drying colloidal suspensions. *Langmuir* 38:7442–47
- Lilin P, Elkhoury JE, Peters IR, Bischofberger I. 2024a. Fracture and relaxation in dense cornstarch suspensions. *PNAS Nexus* 3(1):pgad451
- Lilin P, Ibrahim M, Bischofberger I. 2024b. Crack densification in drying colloidal suspensions. *Sci. Adv.* 10:eadp3746
- Lin-Gibson S, Pathak JA, Grulke EA, Wang H, Hobbie EK. 2004. Elastic flow instability in nanotube suspensions. *Phys. Rev. Lett.* 92:048302
- Liu J, Paul JD, Gollub JP. 1993. Measurements of the primary instabilities of film flows. *J. Fluid Mech.* 250:69–101
- Lohse D. 2018. Bubble puzzles: from fundamentals to applications. *Phys. Rev. Fluids* 3(11):110504
- Luo R, Chen Y, Lee S. 2018. Particle-induced viscous fingering: review and outlook. *Phys. Rev. Fluids* 3:110502
- Luo R, Chen Y, Lee S. 2020. Particle-induced miscible fingering: continuum limit. *Phys. Rev. Fluids* 5:094301
- Mazumder R. 2003. Sediment transport, aqueous bedform stability, and morphodynamics under unidirectional current: a brief overview. *J. Afr. Earth Sci.* 36:1–14
- Meiburg E, Kneller B. 2010. Turbidity currents and their deposits. *Annu. Rev. Fluid Mech.* 42:135–56
- Mendez MA, Scheid B, Buchlin JM. 2017. Low Kapitza falling liquid films. *Chem. Eng. Sci.* 170:122–38
- Meng Y, Li W, Juanes R. 2022. Fracturing in wet granular media illuminated by photoporomechanics. *Phys. Rev. Appl.* 18:064081
- Meng Y, Primkulov B, Yang Z, Kwok C, Juanes R. 2020. Jamming transition and emergence of fracturing in wet granular media. *Phys. Rev. Res.* 2:022012
- Milani M, Phou T, Ligoure C, Cipelletti L, Ramos L. 2023. A double rigidity transition rules the fate of drying colloidal drops. *Soft Matter* 19:6968–77
- Montesi A, Peña Á, Pasquali M. 2004. Vorticity alignment and negative normal stresses in sheared attractive emulsions. *Phys. Rev. Lett.* 92:058303
- Morris JF. 2020. Shear thickening of concentrated suspensions: recent developments and relation to other phenomena. *Annu. Rev. Fluid Mech.* 52:121–44
- Mounkaila N, Dagois-Bohy S, Millet S, Botton V, Henry D, Hadid HB. 2021. Primary instability of a viscoplastic film down an inclined plane: experimental study. *J. Fluid Mech.* 922:R2
- Mounkaila ND, Dagois-Bohy S, Millet S, Ben Hadid H, Botton V, Henry D. 2023. Nonlinear evolution of viscoplastic film flows down an inclined plane. *Eur. Phys. J. E* 46(8):68
- Mueller S, Llewellyn EW, Mader HM. 2010. The rheology of suspensions of solid particles. *Proc. R. Soc. A* 466(2116):1201–28
- Nase J, Derks D, Lindner A. 2011. Dynamic evolution of fingering patterns in a lifted Hele–Shaw cell. *Phys. Fluids* 23(12):123101
- Nesterov O. 2010. Numerical modeling of non-hydrostatic free-surface baroclinic flows induced by suspended particles. In *Environmental Hydraulics*, Vol. 1, ed. GC Christodoulou, AI Stamou. Taylor & Francis
- Olsen K, Flekkøy E, Angheluta L, Campbell J, Måløy K, Sandnes B. 2019. Geometric universality and anomalous diffusion in frictional fingers. *New J. Phys.* 21:063020
- Ozturk D, Morgan M, Sandnes B. 2020. Flow-to-fracture transition and pattern formation in a discontinuous shear thickening fluid. *Commun. Phys.* 3:119
- Padhy S, Shaqfeh ESG, Iaccarino G, Morris JF, Tonmukayakul N. 2013. Simulations of a sphere sedimenting in a viscoelastic fluid with cross shear flow. *J. Non-Newtonian Fluid Mech.* 197:48–60
- Pächtz T, Clark AH, Valyrakis M, Durán O. 2020. The physics of sediment transport initiation, cessation, and entrainment across aeolian and fluvial environments. *Rev. Geophys.* 58(1):e2019RG000679
- Palak, Parmar VRS, Bandyopadhyay R. 2023. Growth kinetics of interfacial patterns formed by the radial displacement of an aging viscoelastic suspension. *JCIS Open* 10:100084
- Palak, Parmar VRS, Saha D, Bandyopadhyay R. 2022. Pattern selection in radial displacements of a confined aging viscoelastic fluid. *JCIS Open* 6:100047
- Park J, Metzger B, Guazzelli E, Butler JE. 2010. A cloud of rigid fibres sedimenting in a viscous fluid. *J. Fluid Mech.* 648:351–62

- Parmar VRS, Bandyopadhyay R. 2024. Interfacial instabilities in confined displacements involving non-Newtonian fluids. *Europhys. Lett.* 145:47001
- Peters IR, Majumdar S, Jaeger HM. 2016. Direct observation of dynamic shear jamming in dense suspensions. *Nature* 532(7598):214–17
- Phillips RJ, Armstrong RC, Brown RA, Graham AL, Abbott JR. 1992. A constitutive equation for concentrated suspensions that accounts for shear-induced particle migration. *Phys. Fluids* 4:30–40
- Roché M, Myftiu E, Johnston MC, Kim P, Stone HA. 2013. Dynamic fracture of nonglassy suspensions. *Phys. Rev. Lett.* 110(14):148304
- Roht YL, Ippolito I, Hulin J-P, Salin D, Gauthier G. 2018. Stripes instability of an oscillating non-Brownian iso-dense suspension of spheres. *Europhys. Lett.* 121(5):54002
- Routh AF. 2013. Drying of thin colloidal films. *Rep. Prog. Phys.* 76:046603
- Roshko A. 1954. *On the development of turbulent wakes from vortex streets*. Rep. 1191, National Advisory Committee for Aeronautics
- Saffman P, Taylor G. 1958. The penetration of a fluid into a porous medium or Hele-Shaw cell containing a more viscous liquid. *Proc. R. Soc. A* 245:312–29
- Saint-Michel B, Manneville S, Meeker S, Ovarlez G, Bodiguel H. 2019. X-ray radiography of viscous resuspension. *Phys. Fluids* 31(10):103301
- Sandnes B, Flekkøy E, Knudsen H, Maloy K, See H. 2011. Patterns and flow in frictional fluid dynamics. *Nat. Commun.* 2:288
- Shields A. 1936. *Application of similarity principles and turbulence research to bed-load movement*. Rep., Soil Conservation Service Cooperative Laboratory, California Institute of Technology
- Snabre P, Mills P. 2000. Settling and fluidization of non-Brownian hard spheres in a viscous liquid. *Eur. Phys. J. E* 1:105–14
- Tang H, Grivas W, Homencovschi D, Geer J, Singler T. 2000. Stability considerations associated with the meniscoid particle band at advancing interfaces in Hele-Shaw suspension flows. *Phys. Rev. Lett.* 85:2112–15
- Taylor GI. 1923. Stability of a viscous liquid contained between two rotating cylinders. *Philos. Trans. R. Soc. A* 223:289–343
- Thorens L, Måløy KJ, Flekkøy EG, Sandnes B, Bourgoïn M, Santucci S. 2023. Capillary washboarding during slow drainage of a frictional fluid. *Soft Matter* 19(48):9369–78
- Tamburrino A, Ihle CF. 2013. Roll wave appearance in bentonite suspensions flowing down inclined planes. *J. Hydraul. Res.* 51(3):330–35
- Timberlake BD, Morris JF. 2002. Concentration band dynamics in free-surface Couette flow of a suspension. *Phys. Fluids* 14(5):1580–89
- Tirumkudulu M, Tripathi A, Acrivos A. 1999. Particle segregation in monodisperse sheared suspensions. *Phys. Fluids* 11(3):507–9
- Valance A, Berzi D. 2022. Particle saltation over rigid bumpy beds in viscous shearing flows. *J. Fluid Mech.* 947:A28
- Van Damme H, Lemaire E, Ould Y, Abdelhaye M, Mouchid A, Levitz P. 1994. Pattern formation in particulate complex fluids: a guided tour. In *Non-Linearity and Breakdown in Soft Condensed Matter*, ed. KK Bardhan, BK Chakrabarti, A Hansen. Springer
- van Rijn LC. 1984. Sediment transport, part I: bed load transport. *J. Hydraul. Eng.* 110(10):1431–56
- van Rijn LC. 2020. Erodibility of mud–sand bed mixtures. *J. Hydraul. Eng.* 146(1):04019050
- Varga Z, Grenard V, Pecorario S, Taberlet N, Dolique V, et al. 2019. Hydrodynamics control shear-induced pattern formation in attractive suspensions. *PNAS* 116:12193–98
- Varga Z, Swan JW. 2018. Large-scale anisotropies in sheared colloidal gels. *J. Rheol.* 62:405–18
- Verrelli DI, Koh PTL, Nguyen AV. 2011. Particle–bubble interaction and attachment in flotation. *Chem. Eng. Sci.* 66:5910–21
- Vlassopoulos D, Cloitre M. 2014. Tunable rheology of dense soft deformable colloids. *Curr. Opin. Colloid Interface Sci.* 19:561–74
- Vogel S. 1988. *Life's Devices: The Physical World of Animals and Plants*. Princeton University Press
- Wang D, Liu Q. 2021. Hydrodynamics of froth flotation and its effects on fine and ultrafine mineral particle flotation: a literature review. *Miner. Eng.* 173:107220

- Whorton J, Jones TJ, Russell JK. 2025. Particle settling in a shear-thinning, viscoelastic fluid in the presence of wall effects. *Sci. Rep.* 15(1):4482
- Winterwerp JC. 2006. Stratification effects by fine suspended sediment at low, medium, and very high concentrations. *J. Geophys. Res. Oceans* 111:C5
- Womersley JR. 1955. Method for the calculation of velocity, rate of flow and viscous drag in arteries when the pressure gradient is known. *J. Physiol.* 127(3):553–63
- Wysocki A, Royall CP, Winkler RG, Gompper G, Tanaka H, et al. 2009. Direct observation of hydrodynamic instabilities in a driven non-uniform colloidal dispersion. *Soft Matter* 5(7):1340–44
- Xu F, Kim J, Lee S. 2016. Particle-induced viscous fingering. *J. Non-Newtonian Fluid Mech.* 238:92–99
- Xu F, Lee S. 2019. The enhancement of viscous fingering with bidisperse particle suspension. *J. Fluid Mech.* 860:487–509
- Yu YE, Khodaparast S, Stone HA. 2018. Separation of particles by size from a suspension using the motion of a confined bubble. *Appl. Phys. Lett.* 112:181604
- Zhang D, Campbell J, Eriksen J, Flekkøy E, Maloy K, et al. 2023. Frictional fluid instabilities shaped by viscous forces. *Nat. Commun.* 14:3044